



NRL/MR/5621--00-8516

# **Summer 1999 Mount Weather/Aberdeen Proving Grounds Field Test Report: Real-Time Detection of Military Ground Targets Using a VIS/NIR Hyperspectral Sensor**

FREDERICK M. OLCHOWSKI  
CHRISTOPHER M. STELLMAN  
JOSEPH V. MICHALOWICZ

*Advanced Concepts Branch  
Optical Sciences Division*

November 27, 2000

20001213 146

Approved for public release; distribution is unlimited.

REPORT DOCUMENTATION PAGE			Form Approved OMB No. 0704-0188	
Public reporting burden for this collection of information is estimated to average 1 hour per response, including the time for reviewing instructions, searching existing data sources, gathering and maintaining the data needed, and completing and reviewing the collection of information. Send comments regarding this burden estimate or any other aspect of this collection of information, including suggestions for reducing this burden, to Washington Headquarters Services, Directorate for Information Operations and Reports, 1215 Jefferson Davis Highway, Suite 1204, Arlington, VA 22202-4302, and to the Office of Management and Budget, Paperwork Reduction Project (0704-0188), Washington, DC 20503.				
1. AGENCY USE ONLY (Leave Blank)	2. REPORT DATE November 27, 2000	3. REPORT TYPE AND DATES COVERED Final		
4. TITLE AND SUBTITLE Summer 1999 Mount Weather/Aberdeen Proving Grounds Field Test Report: Real-Time Detection of Military Ground Targets Using a VIS/NIR Hyperspectral Sensor			5. FUNDING NUMBERS	
6. AUTHOR(S) Frederick M. Olchowski, Christopher M. Stellman, and Joseph V. Michalowicz				
7. PERFORMING ORGANIZATION NAME(S) AND ADDRESS(ES) Naval Research Laboratory Washington, DC 20375-5320			8. PERFORMING ORGANIZATION REPORT NUMBER NRL/MR/5621--00-8516	
9. SPONSORING/MONITORING AGENCY NAME(S) AND ADDRESS(ES)			10. SPONSORING/MONITORING AGENCY REPORT NUMBER	
11. SUPPLEMENTARY NOTES				
12a. DISTRIBUTION/AVAILABILITY STATEMENT Approved for public release; distribution is unlimited.			12b. DISTRIBUTION CODE	
13. ABSTRACT (Maximum 200 words)  The following provides an overview of a VIS/NIR hyperspectral sensor system and two recent field experiments in which it was employed. The system hardware components, software interface, and processing methods are described in detail. A description of the test flight experiments and a preliminary analysis of the collected data are given.				
14. SUBJECT TERMS Hyperspectral detection Remote sensing			15. NUMBER OF PAGES 42	
			16. PRICE CODE	
17. SECURITY CLASSIFICATION OF REPORT UNCLASSIFIED	18. SECURITY CLASSIFICATION OF THIS PAGE UNCLASSIFIED	19. SECURITY CLASSIFICATION OF ABSTRACT UNCLASSIFIED	20. LIMITATION OF ABSTRACT UL	

## CONTENTS

EXECUTIVE SUMMARY .....	1
INTRODUCTION .....	1
DATA ACQUISITION SYSTEM .....	2
FIELD DATA .....	15
RESULTS AND DISCUSSION .....	19
SUMMARY .....	25
ACKNOWLEDGEMENTS .....	25
REFERENCES .....	25
APPENDIX I .....	27
APPENDIX II .....	33

## EXECUTIVE SUMMARY

The Mount Weather/Aberdeen Proving Grounds tests have accomplished the following:

- Developed a visible hyperspectral imaging system configured for future use on an unmanned air vehicle
- Successfully integrated the hyperspectral sensor with a high resolution line scanner and a real-time processor
- Demonstrated real-time cueing of high-resolution panchromatic image chips using hyperspectral imaging and subspace RX anomaly detection
- Demonstrated Constant False Alarm Rate(CFAR) anomaly detection
- Collected numerous fully corrected visible hyperspectral data cubes in real-time

## INTRODUCTION

In recent years military reconnaissance and surveillance have greatly benefited through the expanded use of multispectral and hyperspectral sensors by exploiting spectral differences between critical ground targets and local backgrounds as a detection discriminant. Technological advances in computing power, digital imaging and algorithm development have allowed for real-time detection and cueing of anomalies based on this premise. These developments combined with the results of NRL's (MOVIES) [1] and Dark HORSE [2-4] programs, have led to a follow on program to develop a visible hyperspectral imaging system configured for future use on an unmanned air vehicle (UAV). While the sensor system has been configured for the Predator UAV it will provide an enabling technology for numerous other existing and/or future UAVs, Uninhabited Combat Air Vehicles (UCAVs) and/or manned reconnaissance platforms.

The following provides an overview of the hyperspectral sensor system and two recent field experiments in which it was employed. The system hardware components, software interface and processing methods are described in detail. A description of the test flight experiments is given and a preliminary analysis of the collected data is presented.



## DATA ACQUISITION SYSTEM

The hyperspectral sensor system consists of a hyperspectral imager, a high resolution line scanner, a sensor interface computer (SIC), a data processing computer (DPC), a ground station computer (GSC) and a system user interface. A block diagram of the system is shown in Figure 1.

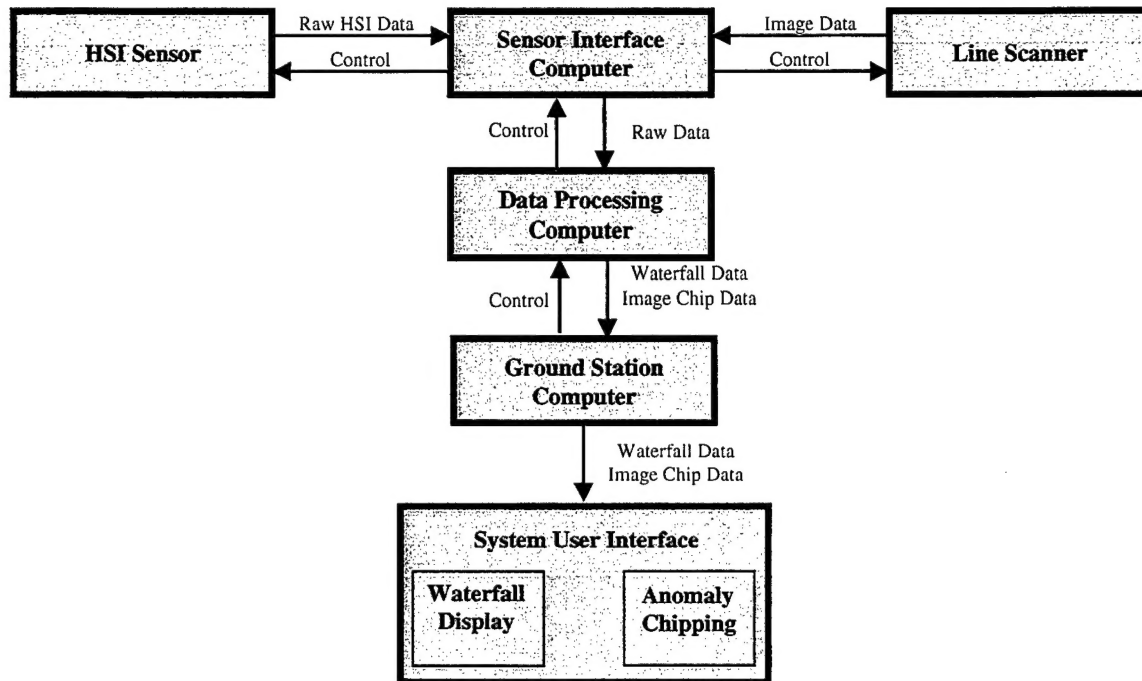


Fig.1 –Block diagram of data acquisition system

### Hyperspectral Sensor

The hyperspectral sensor consists of a Schneider 70mm f/2.2 IR-corrected video camera lens, an American Holographic VS15 f/2.0 dispersive imaging spectrograph and a Pixelvision Pluto back illuminated CCD focal plane array (FPA). The sensor is shown in Figure 2 and its dimensions are shown in Figure 3. During operation, light from the scene is imaged onto the entrance slit of the spectrograph. Light passing through the slit is dispersed and then reimaged onto the FPA. Thus, a hyperspectral image of the entrance slit is created on the FPA with the spatial dimension parallel to the slit and the spectral dimension perpendicular to the slit. Scanning the slit across the scene of interest using aircraft motion gives spatial information in the down-track flight direction and results in a three-dimensional hyperspectral data cube. The FPA consists of 1024 x 1024 pixels with a pitch of 12μm and a depth of 14 bits per pixel. While the FPA is 1024 pixels square, only 512 of the spectral pixels are used

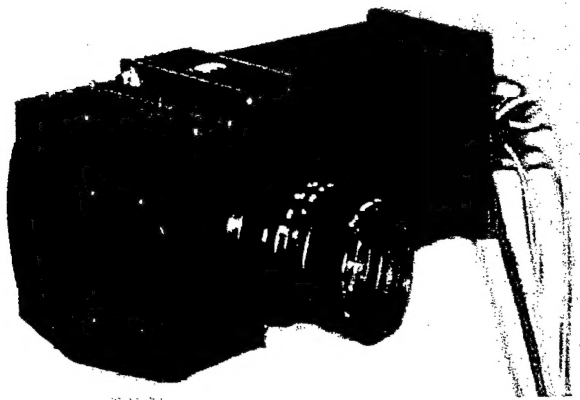


Fig. 2 – Hyperspectral sensor

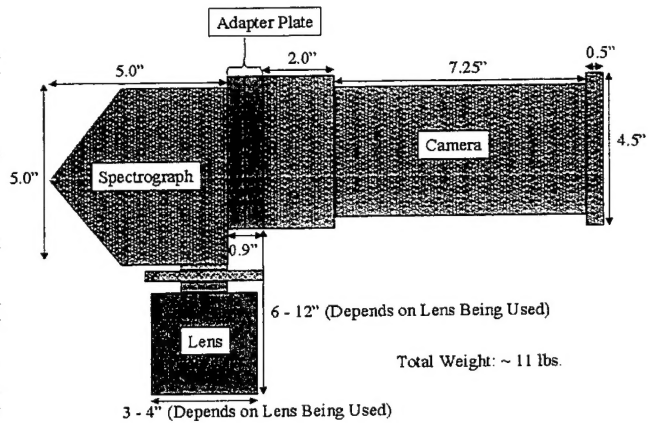


Fig. 3 – Sensor dimensions(topview)

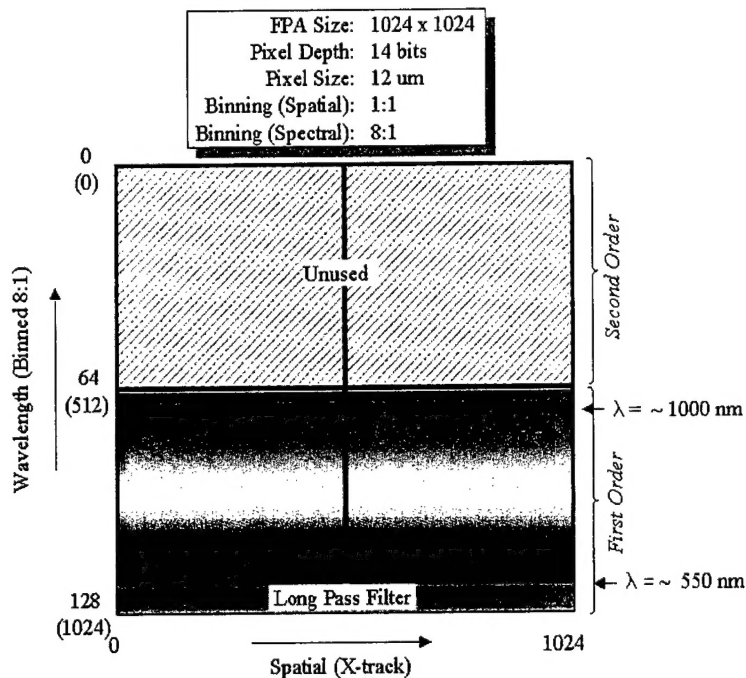


Fig. 4 – Focal plane array dimensions and parameters

corresponding to the first order dispersed light. The second 512 spectral pixels correspond to second order light and are not read out. See Figure 4. In addition to only using half of the spectral pixels, a long pass wavelength filter is employed on the lens to eliminate the shorter wavelength second order light from overlapping the longer wavelengths of the first order. During real-time operation, binning is 8:1 spectrally and 1:1 spatially resulting in 64 wavelength bands and 1024 spatial pixels, respectively. It should also be noted that due to a design error by the spectrograph manufacturer, some vignetting occurs

at the FPA causing the field of view (number of spatial pixels) to be further reduced by approximately 50 pixels on one end of the FPA. The hyperspectral sensor is designed to operate in the visible wavelength regime from 400-1000nm. The spectral resolution of the system is approximately 9.4nm when employing 8:1 spectral binning (required for real-time processing) but is capable of providing a spectral resolution of 1.5nm with 1:1 spectral binning. Thus, during real-time operation, spectral resolution is limited by pixel bin width and not by the width of the entrance slit or FPA pixel size.

The data rate for the hyperspectral sensor is calculated as follows. There are 1024 pixels in the spatial dimension and 30 bands in the spectral dimension with a depth of 2 bytes per pixel, operating at a frame rate of 30 Hz, the data rate is 1.8 MBytes/sec.

$$\text{HSI: } (1024 \text{ pix}) \times (30 \text{ bands}) \times (2 \text{ bytes}) \times (30 \text{ fps}) = 1.8 \text{ MBytes / sec}$$

### **High Resolution Line Scanner**

The high resolution line scanner (Dalsa CL-C8) consists of a one dimensional array of 6000, 10 $\mu$ m square pixels with a pixel depth of 8 bits per pixel. A large format telephoto lens (Pentax 300mm f/4.0), images the scene of interest onto the one dimensional array and an image cube is collected by scanning the array across the scene of interest using aircraft motion.

The data rate for the line scanner is calculated as follows. There are 6000 pixels each with a depth of one byte. Operating at a frame rate of 180 Hz, the data rate is 1.1MBytes/sec.

$$\text{LS: } (6000 \text{ pix}) \times (1 \text{ byte}) \times (180 \text{ fps}) = 1.1 \text{ MBytes / sec}$$

### **Spatial Resolution**

The spatial resolution of both the hyperspectral sensor and the high-resolution line scanner is determined by a combination of hardware limitations and flight parameters. The cross-track and down-track ground sampling distance (GSD) is a function of aircraft altitude, lens focal length and CCD pixel size. In the case of down-track GSD, aircraft speed and camera frame rate must also be factored into the calculation of GSD. For all data presented in this document, the cross-track instantaneous field of view is 160 microradians with a total field of view of 9.4 degrees. A comparison of cross-track GSDs for both cameras at various ranges (altitudes) is plotted in Figure 5. The plots assume that the two cameras have the same total field of view. A typical ground speed is 115 knots with the hyperspectral camera operating at a frame rate of 30Hz. Due to the larger physical array size, the line scanner offers approximately 6x better spatial resolution for a comparable total field of view to that of the hyperspectral camera. This is achieved by means of a large format, long focal length (300mm) lens.

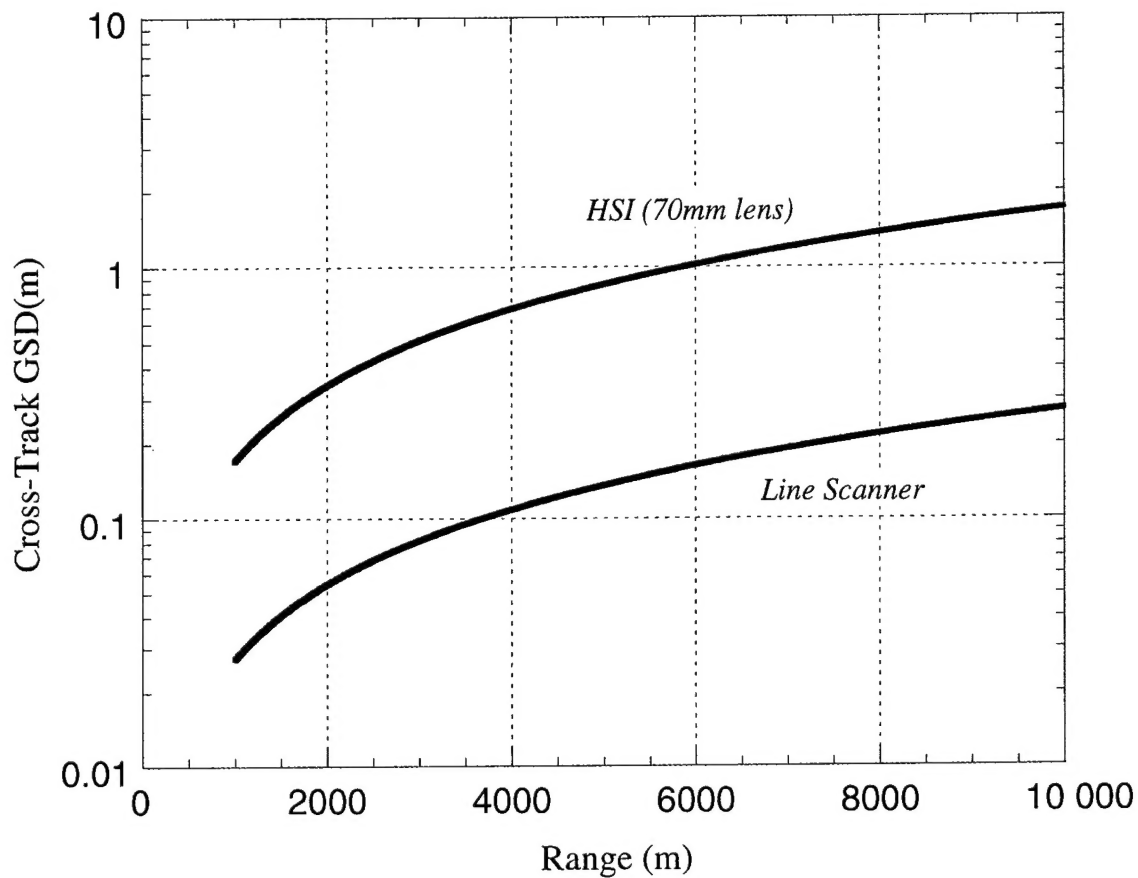


Fig. 5 – Comparison of ground sampling distances (GSD) between the hyperspectral and line scanner cameras.

### Computer System

The computer system consists of three separate computer chassis and a RAID storage system. The sensor interface computer (SIC) contains two frame grabber cards (one for the hyperspectral camera and a second for the line scanner), a 422/232 serial GPS card and a parallel data card for connecting to the data processing computer (DPC). Captured images are sent from the SIC to the DPC via an RS-422 cable. The DPC houses two quad Sharc boards, a RAID controller card and a RS-422 parallel connection to the RAID. The DPC performs all calibration, detection, image chipping and hyperspectral data archiving functions. A 38.4 Gigabyte RAID system provides enough storage for several hours of record time for data from both the hyperspectral sensor and line scanner. The third computer is the ground station computer (GSC). The GSC serves as the primary user interface providing the operator with a three color hyperspectral waterfall display on one monitor and a series of high resolution images of “chipped” anomalies on a second monitor.

## Calibration

Before the anomaly detection algorithm can be run on data acquired by the hyperspectral sensor, the sensor must be flat-fielded, spatially registered and spectrally binned. Flat-fielding corrects for the non-uniformity in pixel-to-pixel photoresponse. Spatial registration eliminates optically-induced image distortions while spectral binning eases the spectral processing requirements of the DPC. A block diagram of the calibration procedure is shown in Figure 6.

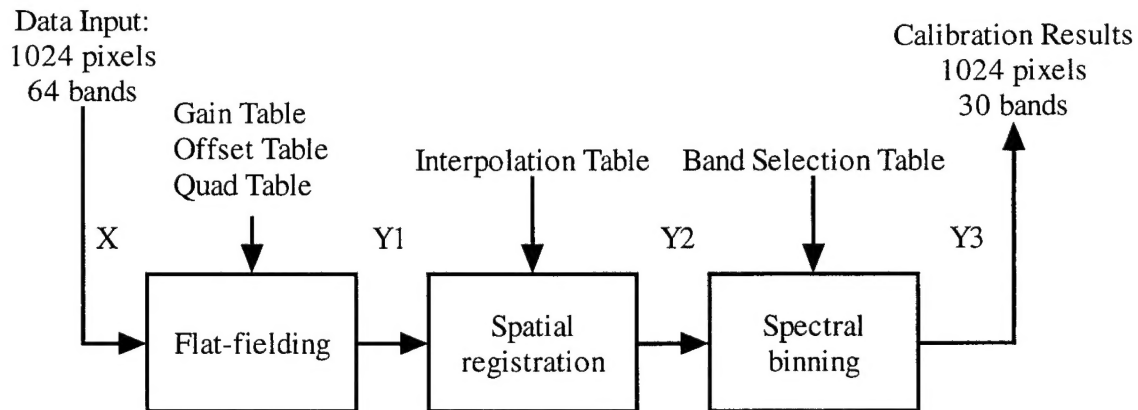


Fig.6 – Calibration block diagram

The first calibration step is flat-fielding of the collected data. Previous analysis of data taken with the PixelVision Pluto camera has shown that there is enough nonlinearity in each pixel's response that a quadratic correction is required to flat-field the sensor. Therefore, prior to flight, three calibration coefficients were derived for each pixel. This was done by focusing the sensor onto the face of the integrating sphere and collecting image frames for various levels of luminance. Thus, a model of each pixel's radiometric response was determined. The model was then used to determine a set of coefficients that could be used to correct for spatial variances in response. Finally a quadratic fit was used to estimate a gain, offset and quadratic coefficient for each pixel. Specifically, for each pixel a quadratic fit was made to a plot of pixel response versus normalized source intensity for the eight luminance settings used. During operation the real-time processor computes the formula (per pixel):

$$Y1 = a + bX + cX^2$$

where  $Y1$  is the pixel response and  $X$  is the normalized source intensity. The coefficients are the offset, " $a$ ", the gain, " $b$ " and the quadratic coefficient, " $c$ ".

After flat-fielding, the collected data is spatially registered to correct for the optical distortion of the spectrograph. The sensor is pointed at a source consisting of twelve broadband light sources aligned in a row. This source is shown in Figure 7. During calibration the sensor is adjusted so that the line of lights is aligned parallel with the sensor slit. Figure 8 shows these lights are evenly spaced in the crosstrack

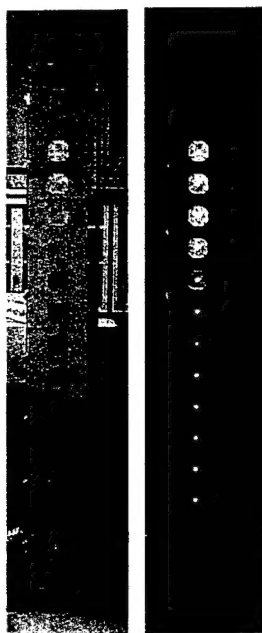


Fig. 7 – Broadband calibration source

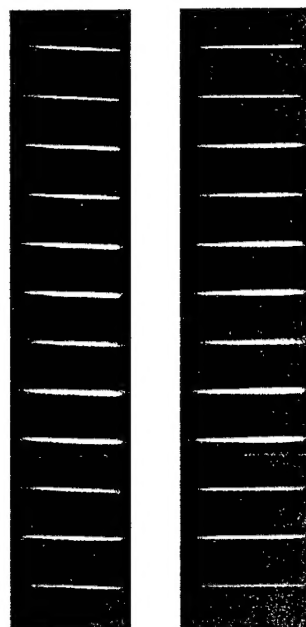


Fig.8 – Spatial misregistration (left) and corrected result (right). The figure on the left is the original 64 bands x 1024 spatial uncalibrated data and that on the right results after a 4-point interpolation registration

direction and extend vertically over most of the spectral dimension (due to the source being broadband). However, it can also be seen that the broadband spectra are originally tilted or not completely vertical. When collecting data, this distortion problem can result in a point source on the ground appearing to shift spatially when viewed in different bands. Thus the problem is often referred to as spatial misregistration.

To correct for this spatial misregistration, code has been developed that takes the data from a laboratory measurement (such as that in Figure 7) and derives a shift value in the crosstrack direction for every pixel in the array ( 64 x 1024 for the sensor). The algorithm employed is a four-point interpolator:

$$Y2(i, j) = \sum_{k=0}^3 h_{S_f}(k) Y1(i - S_i - 2 + k, j)$$

where  $S_i$  and  $S_f$  are the integer and fractional parts of the floating point shift necessary for each pixel. The coefficients,  $h$ , are based on a polynomial interpolator described in reference [1]. The result of applying the correction is also shown in Figure 8(right hand picture).

Lastly, the data is spectrally binned. The real-time processor selectively bins the 64 available bands down to 30 bands and passes the resulting data cube on to the detection algorithm. The binning is selectable in the real-time code and is based on a table passed to the code at run time. The table has thirty entries and each entry has two values: the first is the starting band number and the second is the number of succeeding bands to sum. For the flights presented in this document, we chose to process bands 28 through 57 with no summing.

## Anomaly Detection

The real-time anomaly detection algorithm used is a subspace RX algorithm. The real-time version of the RX algorithm was developed by NRL with the support of SCC, Inc., Santa Monica, CA. The algorithm calculates a recursive mean vector,  $\underline{m}_n$ , and covariance matrix,  $K_n$ , for each pixel using the formulas:

$$\underline{m}_n = (1 - \alpha)\underline{m}_{n-1} + \alpha \underline{z}_n$$

$$K_n = (1 - \alpha)K_{n-1} + \alpha(1 - \alpha)(\underline{z}_n - \underline{m}_{n-1})(\underline{z}_n - \underline{m}_{n-1})^T$$

$$\alpha = 2/(N_{eff} + 1)$$

where  $\underline{z}_n$  is the column vector of spectral components of the  $n^{th}$  pixel and  $N_{eff}$  is the sample average (steady state). Normal RX detection computes a detection result,  $r_n$ , for the  $n^{th}$  pixel using the formula:

$$r_n = (\underline{z}_n - \underline{m}_n)^T K^{-1} (\underline{z}_n - \underline{m}_n)$$

The SCC algorithm uses a variation of RX detection where the inverse covariance matrix,  $K^{-1}$ , is calculated using the formula:

$$K^{-1} = Q\Lambda^{-1}Q^T$$

where  $Q$  is a matrix formed from the eigenvalues of the covariance matrix with the form  $\{Q = [\underline{e}_1 \cdots \underline{e}_J]\}$  and where  $J$  is the number of spectral bands and  $\Lambda$  is a diagonal matrix with elements equal to the eigenvalues of the covariance matrix with the form  $\{\Lambda = diag[\lambda_1 \cdots \lambda_J]\}$ .

Then by defining the principal components,  $\underline{x}_n$ , using the formula:

$$\underline{x}_n = Q^T (\underline{z}_n - \underline{m}_n)$$

we can finally calculate the detection result,  $r_n$ , with the formulas:

$$r_n = (\underline{z}_n - \underline{m}_n)^T Q \Lambda^{-1} Q^T (\underline{z}_n - \underline{m}_n)$$

$$r_n = \underline{x}_n^T \Lambda^{-1} \underline{x}_n$$

$$r_n = \sum_{i=1}^J \frac{|\underline{x}_n(i)|^2}{\lambda_i}$$

where  $\{\underline{x}_n(i); i=1, \dots, J\}$  are the elements of the principal component vector  $\underline{x}_n$ .

### Constant False Alarm Rate Detection

A typical problem that is encountered when examining multiple data sets processed through various spectral anomaly detectors is the inability to quantitatively assess or predict detection performance based on the numerical output of the algorithms. Since detector outputs may vary considerably under different experimental conditions, it is not possible to obtain consistent detection results by selecting a single numerical threshold for a given sensor and algorithm. Rather, it becomes necessary to select a threshold

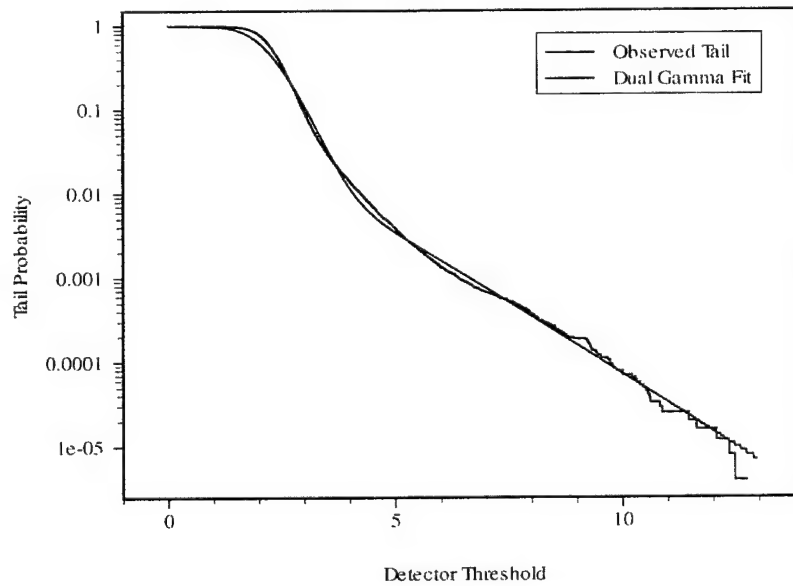


Fig.9 – SSRX detector tail nonlinear least-squares fit. Tail probabilities are presented on a base 10 logarithmic scale.



based on a predictable measure of detector performance. One such measure that is of particular interest in remote sensing studies is the probability of false alarm. This is a technique whereby detector outputs approximating a mixture of  $\chi^2$  distributions can be normalized into constant false alarm rate (CFAR) units, thus allowing the selection of a threshold that yields a consistent probability of false alarm across

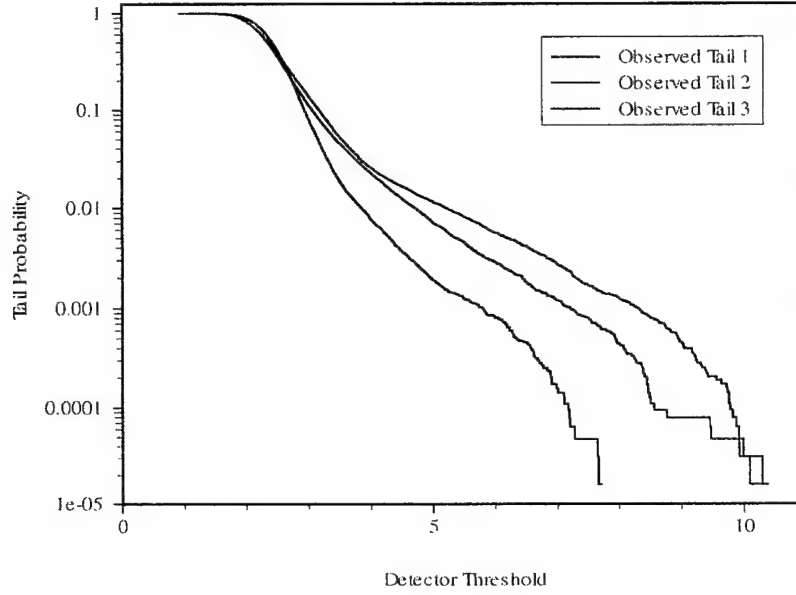


Fig.10 – SSRX detector tails of three different data sets. Detector thresholds correspond to different tail probabilities along each curve.

data sets.

Ideal detector outputs from statistical detection algorithms, such as subspace RX (SSRX) should approximate a known distribution. Algorithms based on RX spectral detection should ideally produce  $\chi^2(k) \equiv \Gamma(k/2, 1/2)$  output, where  $k$  is the number of processed spectral dimensions. However, sensor artifacts and data outliers produce output that is far from ideal, so a more general distribution is required in order to formulate an appropriate model.

A typical SSRX detector tail probability (Figure 9) conforms to a general gamma distribution at lower thresholds, but the extended tail is nearly exponential or  $\Gamma(1, \lambda)$ . This observation motivates a detector distribution based on the mixture of two gammas, where the first gamma models the background clutter and the second models all other scene constituents. The following dual gamma distribution is proposed:

$$Q(t) = w Q_1(t; k_1, \lambda_1) + (1 - w) Q_2(t; k_2, \lambda_2)$$

$$Q_1 \sim \Gamma(k_1, \lambda_1)$$

$$Q_2 \sim \Gamma(k_2, \lambda_2)$$

Where, given any detector threshold  $t \geq 0$ , we may regard the tail probability  $Q(t) = P\{T \geq t\}$  as the probability of false alarm with  $T \sim w \Gamma(k_1, \lambda_1) + (1 - w) \Gamma(k_2, \lambda_2)$ . The parameters  $k_1, \lambda_1, k_2, \lambda_2$  and  $w$  are determined using nonlinear least-squares regression.

For the purpose of detecting targets, it is important to obtain a good fit to the detector tail probability at higher threshold values (i.e., lower false alarm rates). Unfortunately, because higher thresholds correspond to outliers or relatively rare scene constituents, the detector tail probability tends to be very sparse in the region of interest. Therefore, it is necessary to increase the sensitivity of the fitting algorithm to the tail. A simple and effective solution is to fit the logarithm of the tail probability.

Once a suitable dual gamma fit is obtained, the detector data set must be normalized into an operationally useful range. This goal is easily accomplished by transforming each detector threshold  $t$  into its corresponding tail probability  $Q(t)$  under the dual gamma model. Normalized detector tail probabilities approximate an exponential distribution with a constant scale parameter and therefore have a constant false alarm rate (compare Figure 10 with Figure 11).

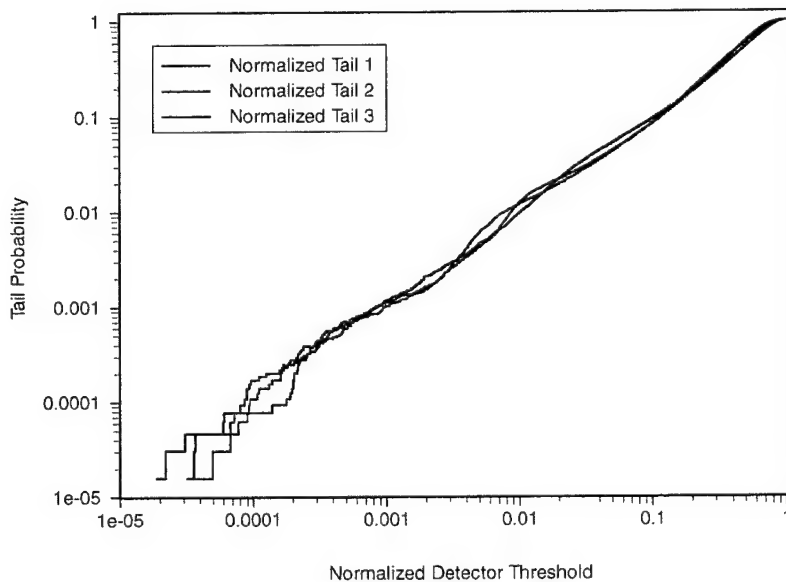


Fig.11 – Normalized SSRX detector tails of the three data sets shown in Figure 10. The exponential tails are linear on a logarithmic scale. Within an acceptable margin of error, normalized detector thresholds correspond to the same tail probability along each curve.

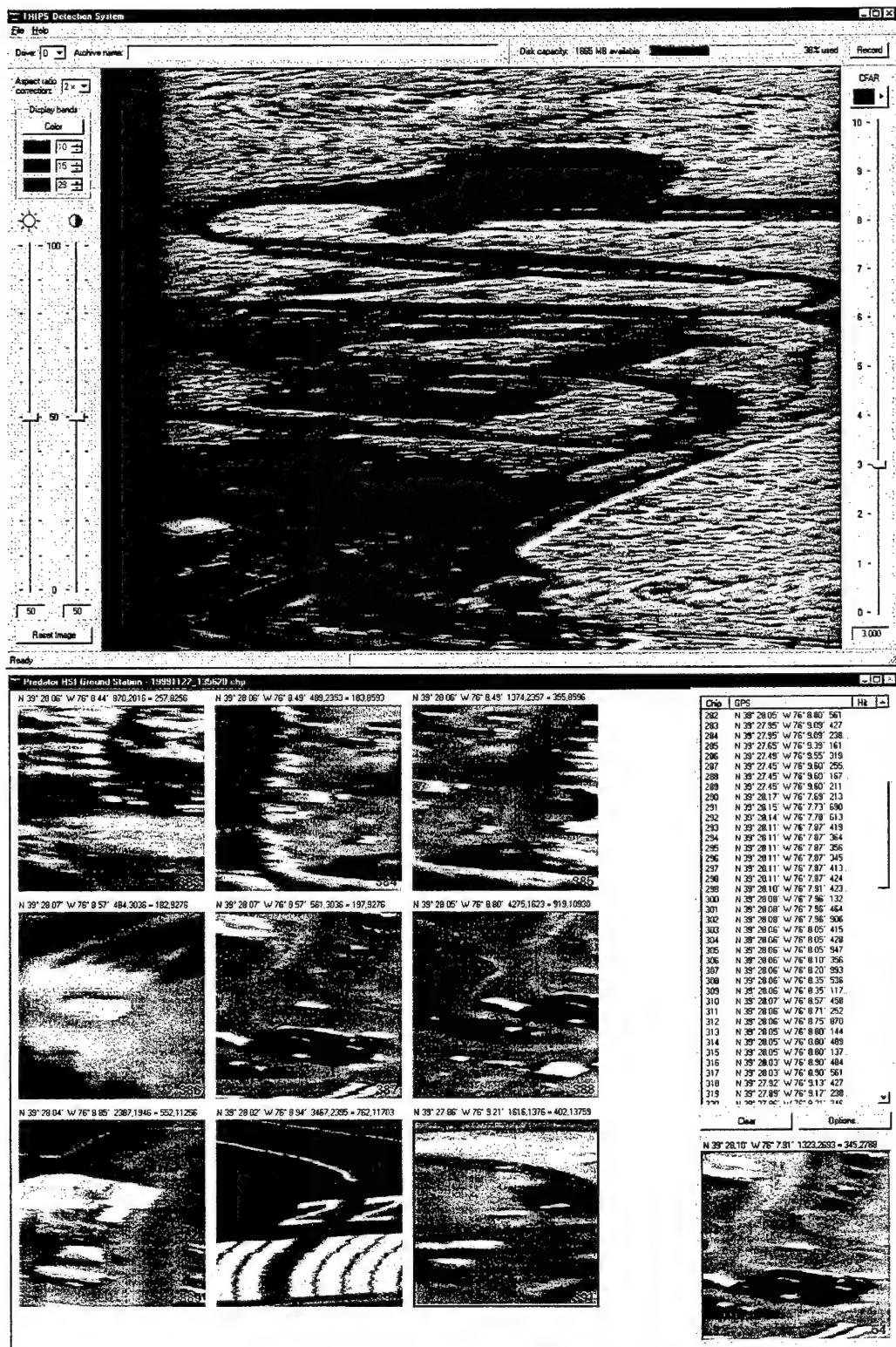


Fig.12 – (Top) Waterfall display with anomalies shown as bright green pixels. (Bottom) Chipped images of detected objects (red boxes in waterfall display)

Since target thresholds typically fall in the range  $10^{-2} < Q(t) < 10^{-4}$ , it is more convenient to specify thresholds in terms of  $-\log_{10}(Q(t))$  or CFAR units. An example of an application where CFAR units are preferable to tail probabilities is a graphical user interface for spectral anomaly detection software (Figure 12).

So that a detector CFAR normalization can be determined, a training stage is run prior to SSRX anomaly detection. This is accomplished by flying over an area that is typical of the background and is as free of anomalies as possible. An anomaly (signal) in this case, spans a broad range of objects that are spectrally different from the rest of the background (clutter). Once the training stage is complete, the CFAR is set by the user. Upon detection, all anomalies are subject to a spatial filter that passes only those cued pixels with appropriate dimensions. If "passed", a box is placed around the object in the waterfall display (Figure 12)-"Top" and a corresponding 256x256 pixel chip from the high resolution line scanner is displayed (Figure 12)-"Bottom". Chipping is constantly updated and only the most recent high-resolution chips are displayed. All chips are saved and may be "highlighted" by the user as being of high, medium or low priority for later viewing by use of the left, middle and right mouse buttons.

### Flight Testing

For flight testing on a U-21 aircraft, both cameras were mounted side by side on a shock mounted phenolic plate, attached to a metal housing crate and inserted into a sensor bay beneath the aircraft (see Figures 14&15). Power supply and fiber optic data cables were routed from the bay into the aircraft cabin



Fig. 13 – U21 aircraft



Fig. 14 – Sensor bay closeup

where rack mounted computers and user interface controls were installed.

Data collection proceeded as follows. With the cameras mounted beneath the aircraft in a nadir pointing direction, images were acquired in a push-broom manner such that the spectrograph entrance slit was perpendicular to the motion of the aircraft. As the aircraft traveled, successive images of the slit built up an image of the target area in a waterfall display. The speed of the aircraft was chosen to be as slow as possible due to the relatively slow frame rate of the hyperspectral camera, to simulate typical operating speeds of a Predator UAV and to prevent pixels from becoming overly elongated in the down-track direction. It should be noted that flying slowly also tended to pitch the aircraft up at a small angle. As a result, the scene being imaged is actually that of the ground slightly forward of the aircraft.

The following table provides an overview of system specifications for the hyperspectral sensor and controller, the high resolution line scanner and the real-time processor. It also lists some typical flight parameters.

Table 1 – Sensor Specifications

<b>Hyperspectral Sensor and Controller</b>	
Spectrometer Type	Imaging Grating, 12 $\mu$ m Slit
Wavelength Range	400-1000nm
Lens	70mm f/2.2 IR Corrected, C-mount
CCD Focal Plane Array	1024 x 1024 Pixels
Pixel Size	12 $\mu$ m <sup>2</sup>
Pixel Depth	14 bit
Frame Rate	50 Hz (30-40 Hz Typical)
<b>High Resolution Line Scanner</b>	
Camera Type	Line Scanner
Wavelength Range	Visible
Lens	Large Format 300mm f/4.0
CCD Array	6000 x 1 Pixels
Pixel Size	10 $\mu$ m <sup>2</sup>
Pixel Depth	8 bit
Frame Rate	Max. 5 kHz (180 Hz Typical)
<b>Real-Time Processor</b>	
Platform	Pentium III, 500 MHz
Algorithm	Subspace RX with Spatial Filtering
<b>Typical Flight Parameters</b>	
Altitude(feet)	6500, 15500
Air Speed	115 knots typical
Hyperspectral Ground Pixel Size	Down-track: 1.5m, 3.2m Cross-track: 0.3m, 0.8m
High Resolution Line Scanner	Down-track: 0.2m Cross-track: 0.06m, 0.15m

## FIELD DATA

Two separate data collections took place in June and August of 1999. The first collection was over both Mount Weather, Virginia and Aberdeen Proving Grounds (APG), Maryland and took place over the course of two days. The second collection also lasted two days but was entirely over Aberdeen Proving Grounds. In each of the collects, numerous military vehicles, trailers, camouflage nets, calibration panels and various cultural objects comprised the target array. GPS coordinates for most of the targets were also provided. Data logs for all flights are shown in Appendix I.

### June Collect

The Mount Weather/APG data was collected June 22-23 under mostly sunny, late morning and mid-afternoon lighting conditions. The target area at Mount Weather was an open field surrounded by forest on three sides and a parking lot and dormitories on the fourth. Military vehicles and camouflage netting were placed along the tree line and included a 5-ton truck and Hummer transport vehicles. A trailer was attached to one of these vehicles and camo netting was placed on two others. Non-military vehicles included two white tractor trailers, and a white truck trailer. A picnic shelter, a concrete pad and the

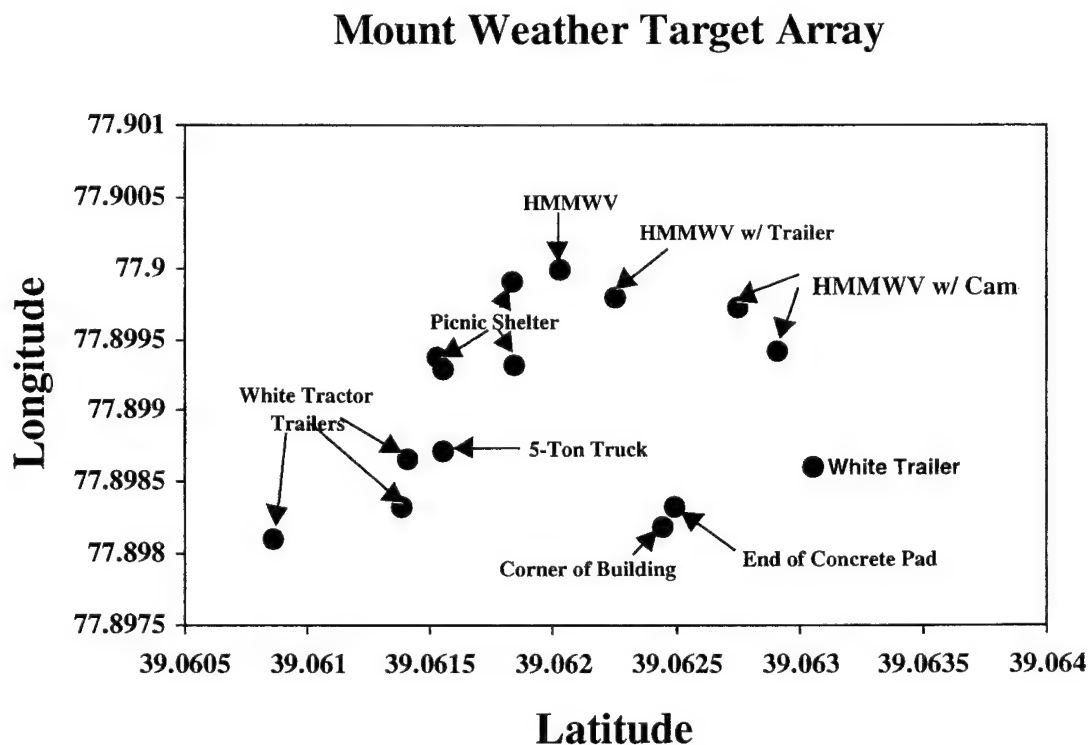


Fig. 15 – Array of targets at Mount Weather site, June 1999

corner of a building were permanent structures whose GPS coordinates were also recorded. Figure 9 shows relative target locations for the array. Photographs of some of the Mount Weather targets are shown in Appendix II.

Only two targets were placed at APG, a FROG-7 rocket launcher and a T-72 Russian tank. Unlike the Mount Weather site where targets could be approached from any direction, APG required a fixed approach due to airspace safety and security issues. The GPS coordinates of the two targets were not recorded. Photographs of some of the Mount Weather targets are shown at the end of this section in Figures 12 and 13.

The sensor system used during the June collects at Mount Weather and APG was a subset of the complete system (Figure 1) subsequently used at APG in August. Only the hyperspectral camera and computers running the real-time algorithm were installed. Image chipping from the Dalsa line scanner was not implemented at this time because the hyperspectral camera itself had not been fully tested. Hyperspectral sensor characterization was the main objective of the June flight tests.

During the June collects, field data was taken at 6500 and 15500 feet with the aircraft heading into the

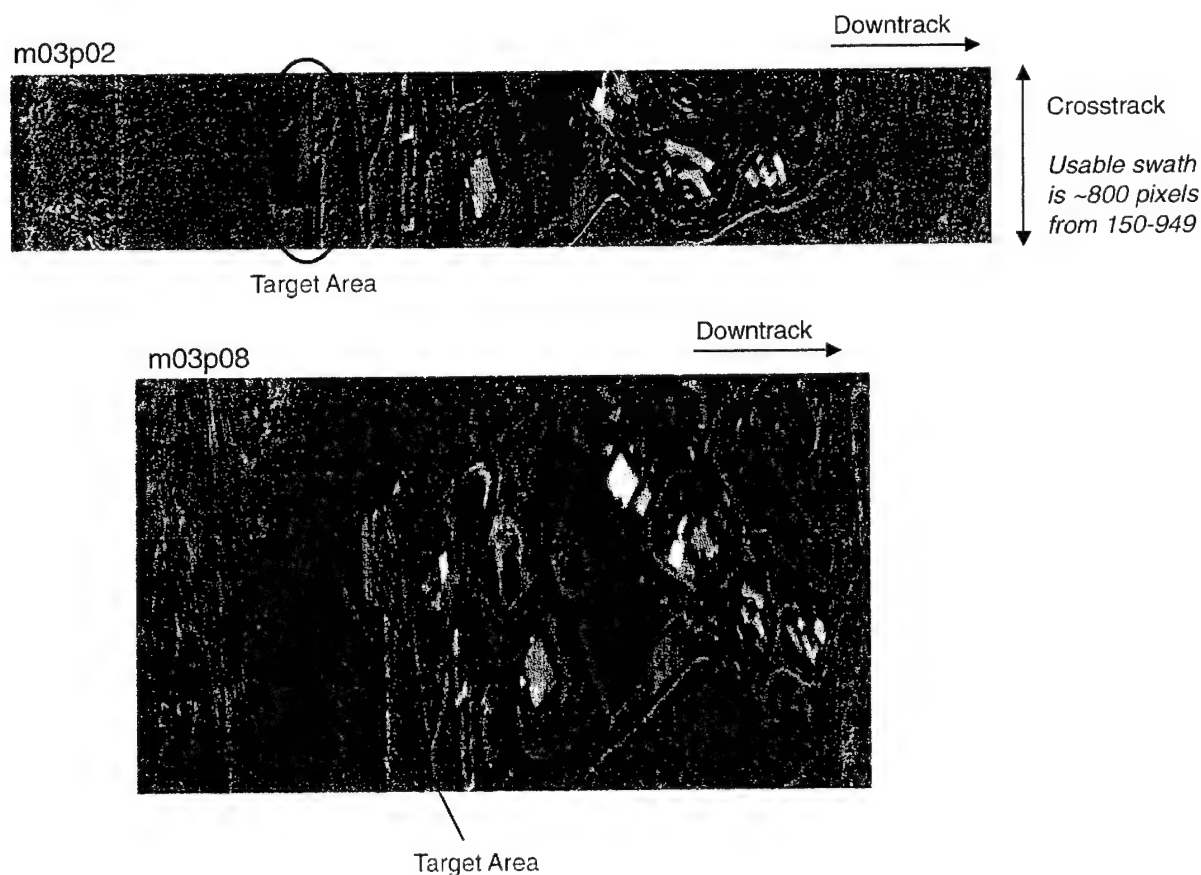


Fig. 16 – Examples of Mount Weather data at 6500(top) and 15500 feet(bottom)



wind to obtain the slowest possible ground speed (85-130 knots). Several passes were made such that the target area was approached from the forested region to obtain good training data prior to encountering the target array. Unfortunately, slow aircraft speeds resulted in significant roll during many of the collected data sets.

Three missions flown in late morning and mid-afternoon resulted in a total of 44 data files. Just over half of the files were collected using the real-time processor. This resulted in fully calibrated data. The rest of the data were uncalibrated raw data sets. When the anomaly detection algorithm was running, only 30 of the 64 bands were recorded. During raw collects, all 64 bands were recorded. A quick look analysis of all data files using the ENVI software package was conducted after each flight to insure that target areas were covered with minimal aircraft roll and that the sensor parameters were correctly set. Examples of data recorded at Mount Weather at 6500 and 15500 feet are shown in Figure 10. The

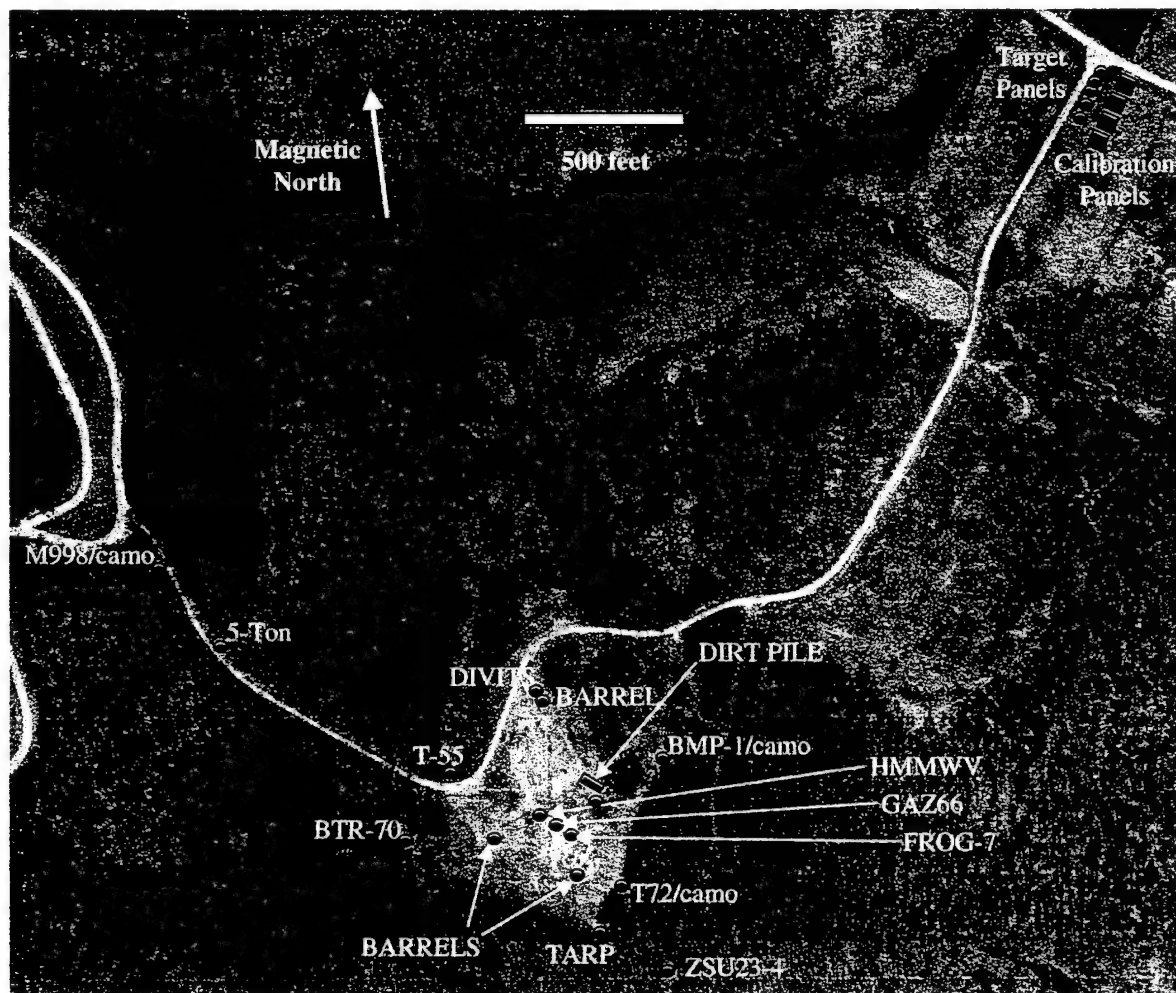


Fig. 17 – Aberdeen Proving Grounds target array, August 1999

dimensions of the upper data set are approximately 250 meters cross-track by 3000 meters down-track.

### **August Collect**

The August 10-11 target array at APG was comprised of a much larger selection of military vehicles than the previous June collect and also included an assortment of calibration panels, tarps and disturbed earth. Targets included IRAQI ZSU-23/4 anti-aircraft artillery, BMP-1 Soviet infantry vehicles, DIVITS, T-72 Russian tanks, M998, BTR-70 Soviet armored vehicles, GAZ 66 Soviet trucks, T-55 tank, Hummer transport vehicles, 5-Ton truck and a FROG-7 rocket launcher. The relative target positions for the array are shown in Figure 11. Many of these vehicles, panels and tarps are shown in Appendix II.

The full sensor system (Figure 1) was used during the August data collects. This included the hyperspectral camera, the high resolution line scanner, and the complete real-time processing system with SSRX anomaly detection and subsequent cued image chipping. A total of 36 files were acquired. Thirty of these files were calibrated data sets collected while running the SSRX anomaly detection algorithm. Six of the collected files were raw data. Altitudes varied from 6500 to 15500 feet. Unfortunately cloud cover was prevalent for a majority of the missions at 15500 feet. Airspeeds were comparable to the missions conducted in June. Due to the requirement to fly at lower altitudes and the relatively slow 30Hz frame rate of the hyperspectral camera, pixels were elongated with down-track to cross-track aspect ratios of 7:1 and 4:1 at 6500 and 15500 feet, respectively. The cross-track GSDs were 0.3 meters and 0.8 meters at 6500 and 15500 feet, respectively. Typically the number of frames captured for each pass was between 400 and 3000 giving a down-track swath between 800 and 6000 meters.

The high resolution Dalsa line scanner operated at a 180 Hz frame rate with a cross-track GSD of 0.05 meters at 6500 feet and 0.15 meters at 15500 feet. The Dalsa linescan pixels were also elongated with the same relative aspect ratios as the hyperspectral sensor.

## RESULTS AND DISCUSSION

Due to cloud cover and other adverse environmental conditions during the August Aberdeen flights, the June Mount Weather/APG data was found to be of better quality. Therefore, analysis has focused on the June data and that is what is discussed here. A preliminary analysis of the data is presented below. Data sets taken at 6500 and 15500 feet are shown in the previous section (Figure 10). A close-up, broadband image of the circled target area is shown in Figure 18 along with a RGB principal component

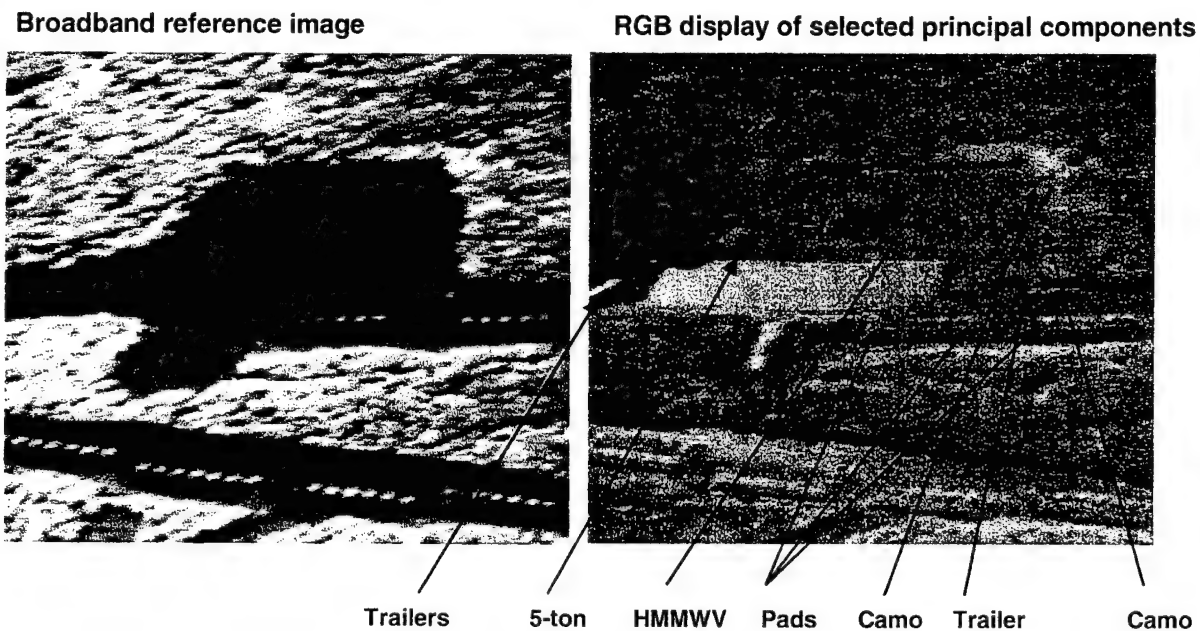


Fig. 18 – Mount Weather target site in broadband(left) and principal components(right) with target positions indicated

image indicating relative positions of targets of interest.

The plots in Figure 19 indicate that the sensor performance is good. By plotting the square root of the first 30 principal components, the clutter-limited modes can easily distinguished from noise-limited modes. By back-projecting the noise limited modes to 30-band space an estimate of the noise floor can be obtained. The resulting RMS spectral noise estimate is more than two orders of magnitude smaller than the spectral mean giving an estimated spectral SNR of approximately 500.

While the in-flight spectral calibration provided a flat field that looked “good to the eye”, a spectral color variation in the cross-track dimension can be noticed upon observing the leading order principal components. The color variation takes the form of a shading artifact that is seen in several of the

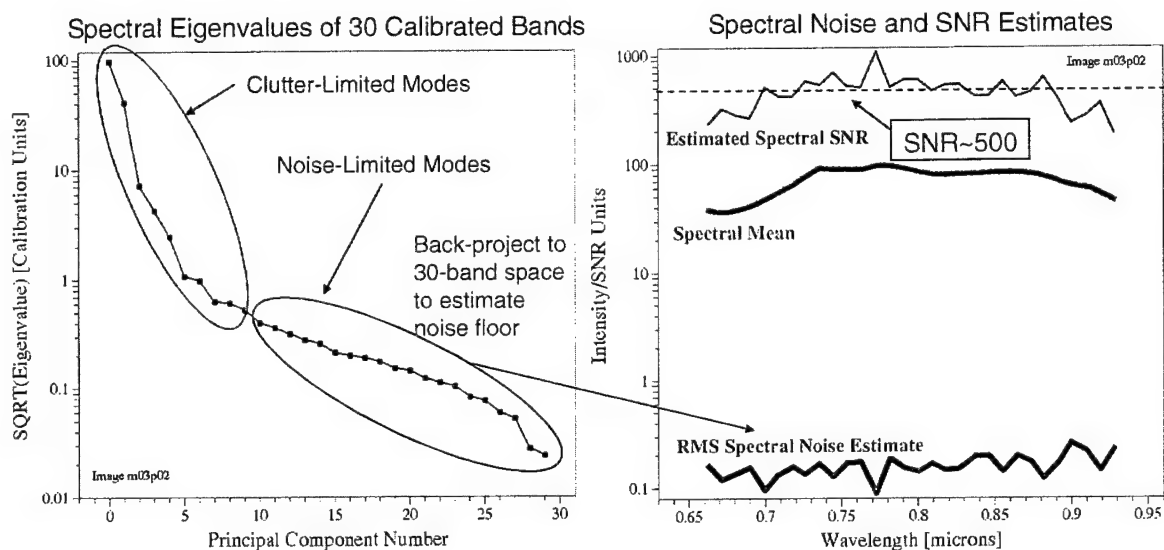
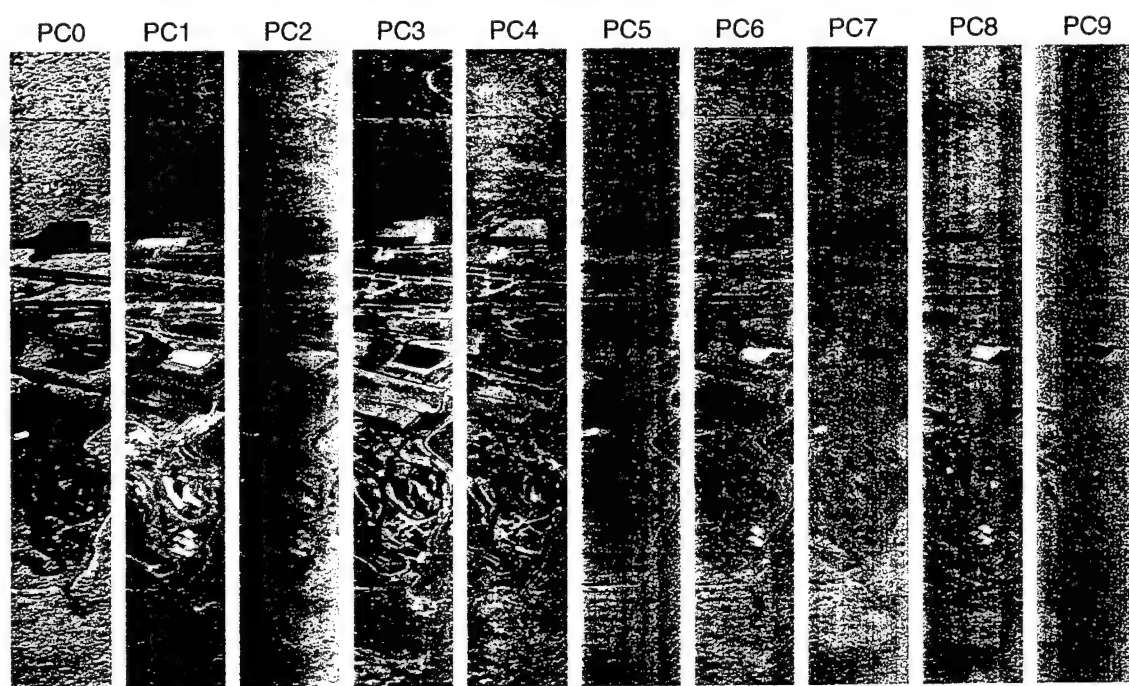


Fig. 19 – Hyperspectral sensor performance



"Shading" artifacts due to crosstrack color change are evident in several PC images (e.g., 2,4,5,9)

Fig. 20 – Principal components of in-flight calibrated data. Shading is prominent in many of these components.

**False Color  
RGB Image**



800 pixels

**NDVI Green  
Vegetation  
Map**

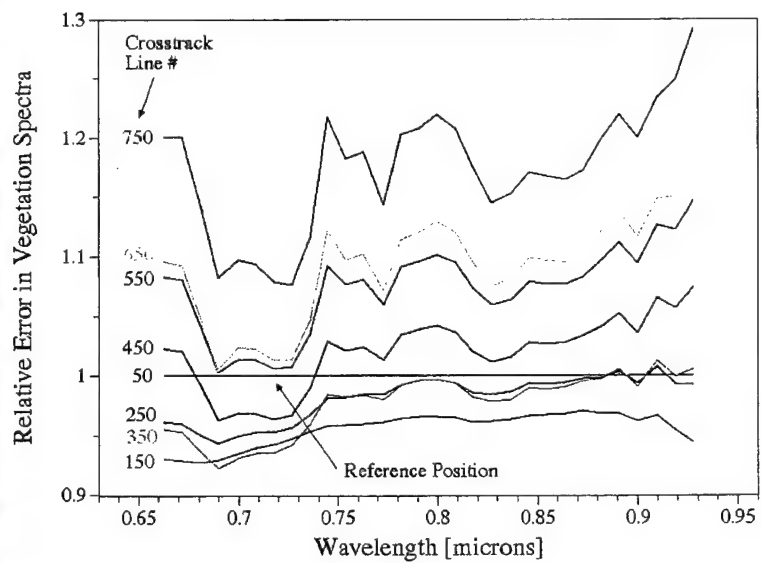
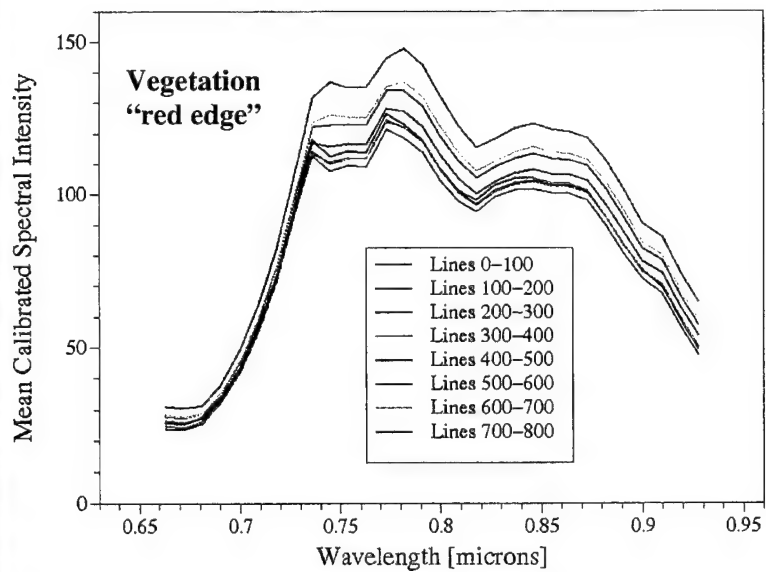


Fig. 21 – Indications of spectral variations in cross-track dimension

components in Figure 20. Further analysis indicates that the mean spectra of the pixels along the cross-track dimension are significantly different on both sides of the swath. Figure 21 shows the normalized difference vegetation index (NDVI) map which is essentially a map of the green vegetation content of each pixel. It is seen that even in cross-track swaths where there is nothing but vegetation, there is a distinct difference in the NDVI on the left and right hand sides. The upper plot in Figure 21 is the mean calibrated spectral intensity of eight, 100 pixel bins of a swath of vegetation. Variations in spectra are largest on the right side of the swath. The lower plot uses line 50 near the left hand side of the swath as a reference to calculate the relative error in these vegetation spectra. It is apparent that the differences are not just illumination scaling but a result of color change.

To fix the spectral variation, a scene-based recalibration has been employed. By measuring the relative change in green vegetation intensity along the cross-track position for each of the 30 bands, the in-flight spectral calibration is gain corrected. The relative change for all bands is plotted in Figure 22 using pixel 50 as the reference. By applying the gain to the original data cube and then examining the image principal components (Figure 23), it is evident that the recalibration has removed the shading artifacts (color variations) present in the original flight calibrated data.

Figure 24 (top) shows an RGB display of another hyperspectral data set. Figure 24 (bottom) is the SSRX anomaly detection results, showing the anomalous pixels in red. Green boxes indicate those anomalies that have also passed the size requirement of the spatial filter. It should be noted that the SSRX anomaly output not only reveals the targets but also several false alarms. Of the false alarms, 14 are small cultural objects and 45 are natural objects. Figure 25 is the same data set, but it has undergone the aforementioned scene-based recalibration. The false alarms are significantly reduced to eight cultural objects and eleven natural objects while all targets remain.

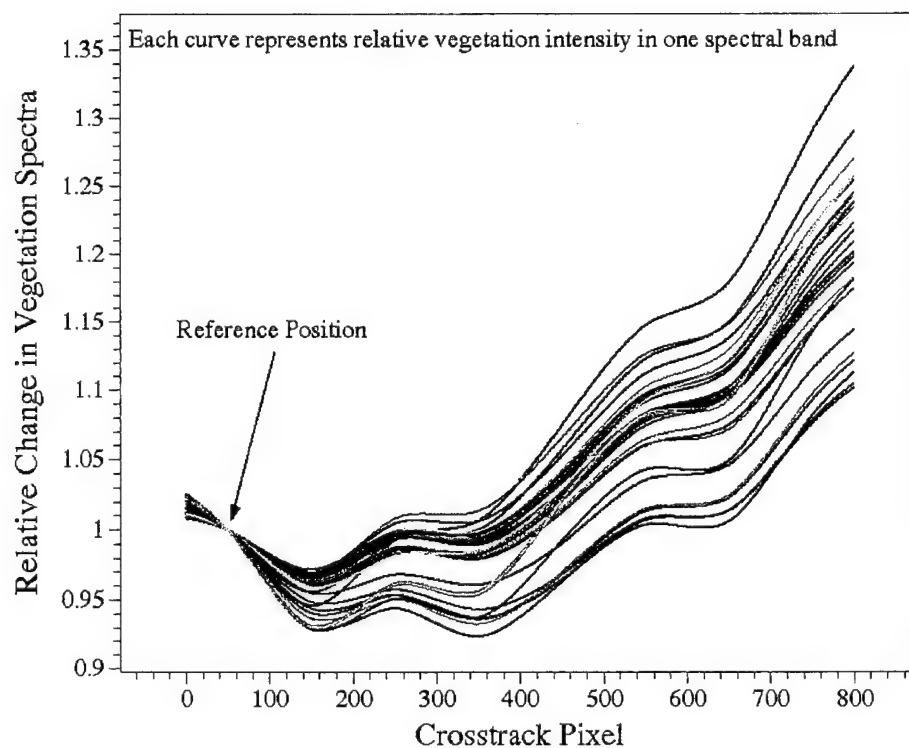
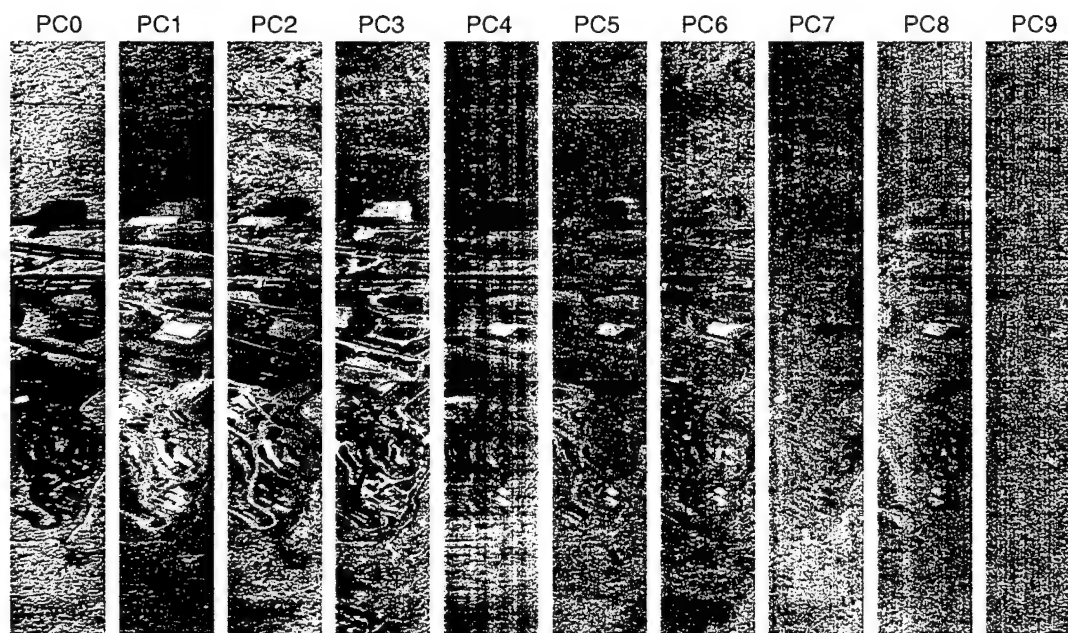


Fig. 22 – Gain correction of spectral bands

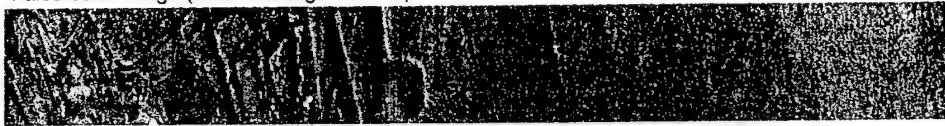


Scene-based recalibration significantly reduces "shading" artifacts in leading-order PC images

Fig. 23 – Principal components from scene based recalibration. Shading artifact is corrected.

Anomaly Detection Test Results:  
Flight-Calibrated 30-Band Image m02p04

False-color image (area coverage ~1 km<sup>2</sup>)



SSRX anomaly detector output with thresholded pixel hits (red) and final cue overlays (green boxes)

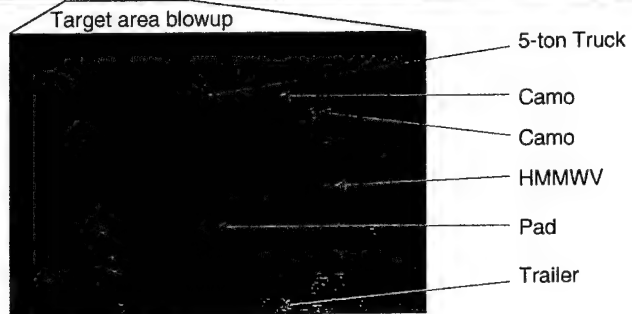


Fig. 24 – In-flight calibration of anomaly detection at Mount Weather site with targets indicated and a significant number of false alarm cues

Anomaly Detection Test Results:  
Re-Calibrated 30-Band Image m02p04

False-color image (area coverage ~1 km<sup>2</sup>)



SSRX anomaly detector output with thresholded pixel hits (red) and final cue overlays (green boxes)

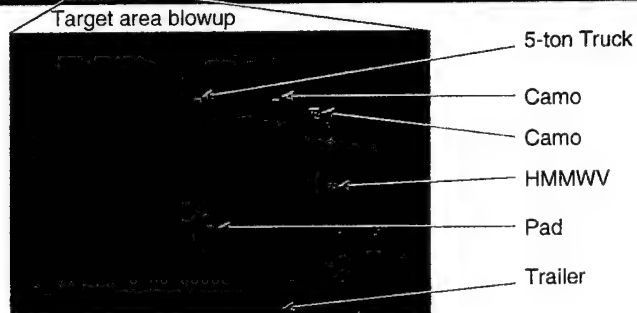


Fig. 25 – Recalibrated anomaly detection at Mount Weather site. False alarms are significantly reduced.



## **SUMMARY**

Successful integration of a VIS/NIR hyperspectral sensor and high resolution line scanner with real-time anomaly detection and image chipping has been accomplished. Good sensor performance is indicated by the low level of striping and the high SNR in the collected images. Numerous fully corrected visible hyperspectral data cubes have been collected in real-time. Real-time cueing of high-resolution panchromatic image chips using hyperspectral imaging and subspace RX anomaly detection has been demonstrated. A spectral color variation has been observed in the cross-track dimension of the leading order principal components but it has been shown that this can be corrected through a post-flight scene based recalibration. Upon doing so, false alarms are significantly reduced.

## **ACKNOWLEDGEMENTS**

Many people contributed to the success of this effort. Software and system integration could not have been possible without the help of William Schaff and Eskander Ensafi of Space Computer Corporation (SCC). Alan Stocker, also of SCC, was instrumental in analyzing the data and providing a method of correcting calibration problems and assessing the performance of the system in general. Installation of the sensor system on the U-21 was made through the efforts of Michael Phillips and Kevin Saltz of SAIC. William Schaffer of SAIC aided in calibration testing and quick-look post flight analysis.

## **REFERENCES**

- [1] "Multispectral Field Measurements for the Multispectral Overhead IR/EO Surveillance Program," W. Shaffer, A. Schaum, E. Ashton, M. McHugh and J.V. Michalowicz, NRL Formal Report 5621-96-9831, 13 September 1996.
- [2] "Real-Time Hyperspectral Detection and Cueing," C.M. Stellman, F. Bucholtz, G.G. Hazel, D. Brown, G. Lynn and J.V. Michalowicz, Submitted to Optical Engineering, January 1999.
- [3] "Hyperspectral Reconnaissance Experiment at Visible Wavelengths with Real-Time Detection and Cueing (Dark HORSE 1)," C.M. Stellman, F. Bucholtz, G.G. Hazel and J.V. Michalowicz, Proceedings of the 1998 Meeting of the IRIS Specialty Group on CC&D, In Press, January 1999.

[4] "Dark HORSE 2 Quick-Look Report: Real-Time Detection of Military Ground Targets Using an Infrared Hyperspectral Imaging Sensor," C.M. Stellman, F. Bucholtz and J.V. Michalowicz, NRL Formal Report 5621-99-8364, 15 April 1999.

[5] "Adaptive Multiple-Band CFAR Detection of an Optical Pattern with Unknown Spectral Distribution," I.S. Reed and X. Yu, IEEE Transaction on Acoustics, Speech and Signal Processing, Vol.38, No. 10, October 1990.

# APPENDIX I

## FLIGHT LOGS

Sunny day, a few clouds					
File(EST)	Gnd. Speed (knots)	Direction (heading)	Alt. (feet)	Comments	
m01p01(no file)	87	080	6500	no file(computer glitch), CFAR=3.0, flying into the wind, calibrated data	
m01p02_19990622_114914.trpa	87	080	6500	missed it, calibrated data	
m01p03_19990622_115438.trpa	87	080	6500	got it, CFAR=1.5, calibrated data	
m01p04_19990622_120115.trpa	87	080	6500	got it, CFAR=1.0, calibrated data	
m01p05_19990622_120901.trpa	87	080	6500	aircraft rolled a bit, waterfall displayed smeared out, calibrated data	
m01p06_19990622_121546.trpa	87	080	6500	got it, calibrated data	
m01p07(no file)	87	080	6500	missed it, raw data collect	
m01p08_19990622_122901.raw	87	080	6500	got it, raw data collect	
m01p09_19990622_125019.trpa	110	080	15500	change altitude, calibrated data, CFAR=1.0, big file	
m01p10_19990622_125603.trpa	110	080	15500	got it, calibrated data, CFAR=0.8	
m01p11_19990622_130144.trpa	110	080	15500	targets blurred due to aircraft roll	
m01p12_19990622_130717.raw	110	080	15500	raw data collect	
m01p13_19990622_131303.raw	110	080	15500	raw data collect, aircraft rolled	
m01p14_19990622_131826.raw	110	080	15500	raw data collect, aircraft rolled slightly	

Morning, sunny with a few clouds					
File(EST)	Gnd. Speed (knots)	Direction (heading)	Alt. (feet)	Comments	
m02p01_19990623_084412.trpa	100	270	6500	don't know if we got the target area, CFAR=3.0, calibrated data	
m02p02_19990623_085337.trpa	95	270	6500	still looking for target area	
m02p03_19990623_085953.trpa	95	270	6500	got it, good pass	
m02p04_19990623_090630.trpa	95	270	6500	got it, CFAR=2.0, calibrated data	
m02p05_19990623_091234.trpa	95	270	6500	missed it	
m02p06_19990623_091928.trpa	95	270	6500	over calibration panel, don't know if we got the whole panel area	
m02p07_19990623_092610.raw	95	270	6500	got it, raw data collect, calibration panels	
m02p08_19990623_093305.raw	95	270	6500	got it, target area	
m02p09_19990623_095531.trpa	95	270	15000	change altitude, calibrated data, CFAR=10, just missed it	
m02p10_19990623_100154.trpa	100	270	15000	rolled a bit over targets, calibrated data, CFAR=2.0	
m02p11_19990623_100745.trpa	100	270	15000	good pass over target area	
m02p12(no file)	100	270	15000	computer glitch(no file)	
m02p13_19990623_101921.raw	100	270	15000	raw data collect, aircraft rolled at target area	
m02p14_19990623_102529.raw	100	270	15000	raw data collect, aircraft rolled slightly	
m02p15_19990623_103205.raw	100	270	15000	raw data collect, aircraft roll	

Mid-afternoon, sunny with a few clouds					
File(EST)	Gnd. Speed (knots)	Direction (heading)	Alt. (feet)	Comments	
m03p01_19990623_151154.trpa	95	90	6500	clouded over at target area	
m03p02_19990623_151808.trpa	95	90	6500	good pass, calibrated data	
m03p03_19990623_152342.trpa	95	90	6500	good pass, calibrated data	
m03p04_19990623_153033.raw	95	90	6500	a little cloudy but we might have it, raw data collect	
m03p05_19990623_153554.raw	95	90	6500	good pass but aircraft rolled a bit	
m03p06_19990623_154748.raw	95	90	6500	good pass, lots of trees before target area	
m03p07_19990623_155406.raw	95	90	6500	good pass	
m03p08.trpa	95	90	15500	CFAR=2.0, good pass, got it	
m03p09.trpa	95	90	15500	good pass	
m03p10_19990623_162917.raw	95	90	15500	good pass, a few light clouds	
m03p11_19990623_163443.raw	95	90	15500	over target area, but aircraft pitched and waterfall display halted for a few frames	
m03p12_19990623_164019.raw	95	90	15500	rolled, but a good pass	
m03p13_19990623_164626.raw	115	90	15500	speeding up, good pass with a few clouds toward the end	
m03p14_19990623_165200.raw	118	90	15500	okay, but waterfall display hesitated over the target area	
m03p15_19990623_170348.raw	118	90	15500	clouds obscured the target area	
m03p16_19990623_170348.raw	118	90	15500	don't know if we got the target area	

Overcast skies					
File(year-date-timeEST)	Gnd. Speed (knots)	Direction (heading)	Alt. (feet)	Comments	
19990810_095946.prda	115	-	6500	checking system	
19990810_100910.prda	115	-	6500	checking system	
boresight_1.raw	115	-	6500	checking system	
boresight_2.raw	115	-	6500	checking system	
19990810_102609.prda	115	-	6500	checking system	

Overcast skies				
File(year-date-timeEST)	Gnd. Speed (knots)	Direction (heading)	Alt. (feet)	Comments
19990810_145322.prda	115	040	11500	good pass, calibrated data
19990810_145800.prda	115	040	11500	good pass, calibrated data
vibration_low.raw	75	250	11500	good pass, raw data collect
vibration_high.raw	75	250	11500	good pass, raw data collect
19990810_151834.prda	75	250	11500	good pass, calibrated data
19990810_152909.prda	95	220	11500	good pass, calibrated data
19990810_153016.prda	95	220	11500	good pass, calibrated data
19990810_153721.prda	95	220	11500	good pass, calibrated data
19990810_153952.prda	90	250	11500	good pass, calibrated data
19990810_155205.prda	90	250	11500	good pass, calibrated data
afternoon_0810_5pm.raw	90	250	11500	good pass, raw data collect
afternoon510pm.raw	90	250	11500	good pass, raw data collect
19990810_160947.prda	90	250	11500	good pass, calibrated data
19990810_161139.prda	90	250	11500	good pass, calibrated data

Hazy, lots of clouds				
File(year-date-timeEST)	Gnd. Speed	Direction (heading)	Alt. (feet)	Comments
19990811_102427.prda	105	040	15500	no test
19990811_102821.prda	105	040	15500	good pass
19990811_103134.prda	95	270	15500	missed targets
19990811_103552.prda	95	270	15500	computer rebooted
19990811_104148.prda	95	270	15500	good pass
19990811_104935.prda	95	270	15500	good pass
19990811_105635.prda	110	270	15500	good pass
19990811_110330.prda	110	270	15500	good pass
boresight_wed.raw	95	270	15500	raw collect
19990811_142455.prda	95	270	15500	clouds obscured targets
19990811_143107.prda	95	270	15500	slight clouds
19990811_145944.prda	95	270	15500	clouds
19990811_150721.prda	110	270	6500	changing computer code
19990811_151431.prda	110	040	6500	software crash
19990811_152308.prda	110	040	6500	calibration panels
19990811_154335.prda	110	270	6500	missed targets
19990811_154530.prda	110	270	6500	clouds
19990811_155248.prda	110	270	6500	good pass



## Appendix II

### TARGETS

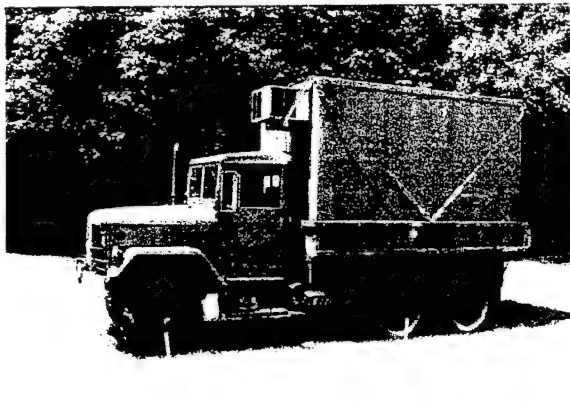
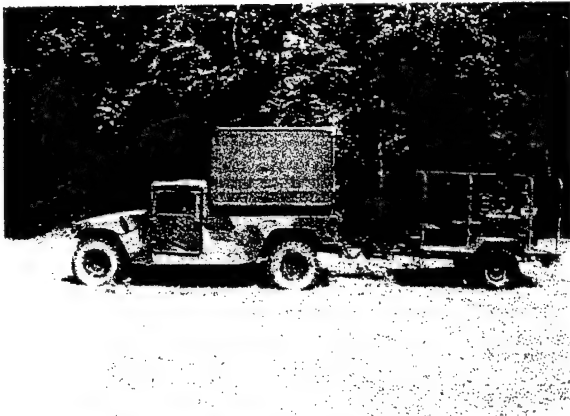
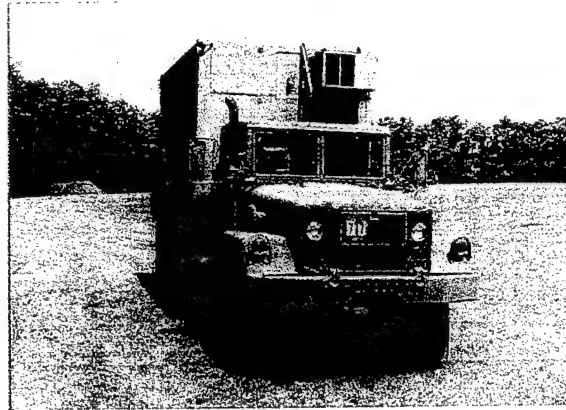


Figure 1: Mount Weather target vehicles

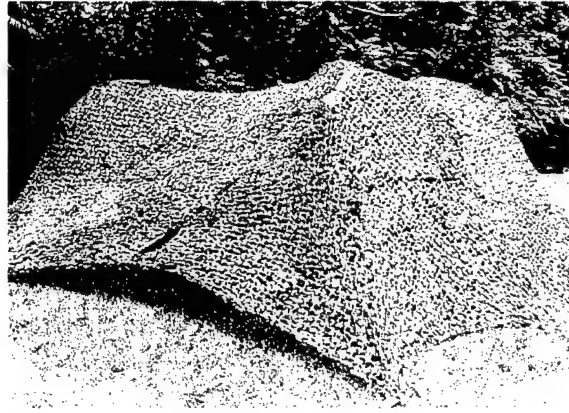


Figure 2: Mount Weather camouflage nets

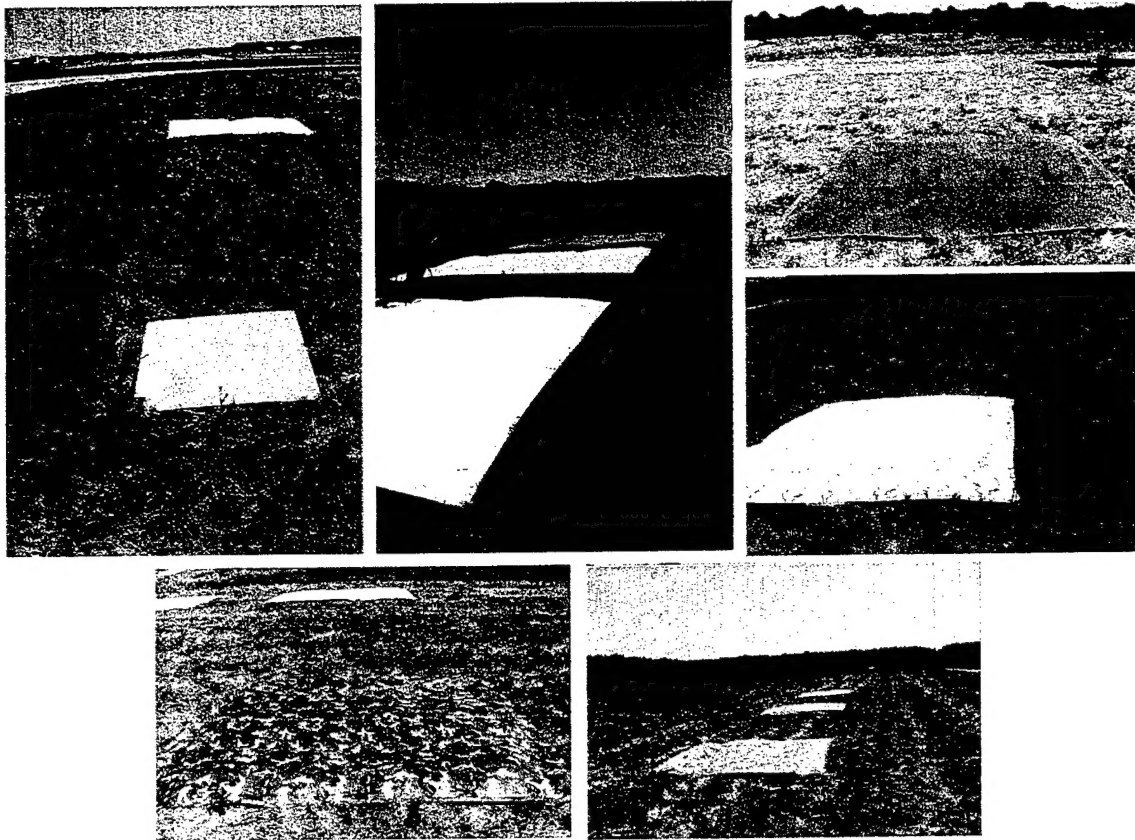


Figure 3: Calibration and target panels used at APG in August, 1999



Figure 4: Target vehicles in woods at APG in August, 1999



Figure 5: Camouflaged and hidden target vehicles at APG in August, 1999

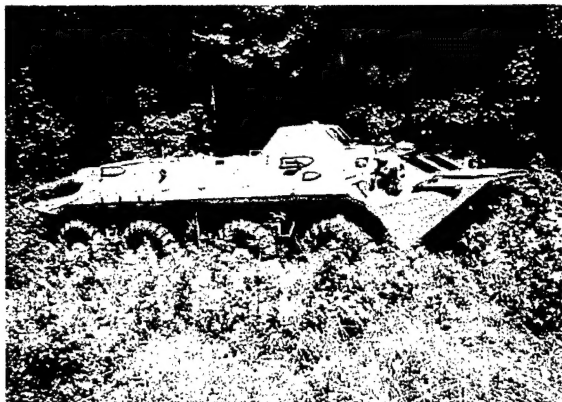
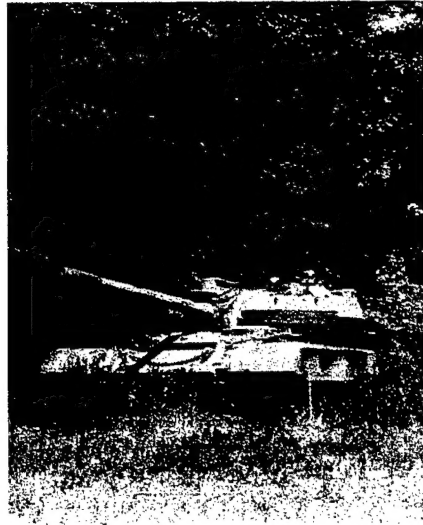


Figure 6: Camouflaged and hidden vehicles at APG in August, 1999